Creep-fatigue Design Based on the Analyses of Thermal Stress-strain Concentration for Simplified Turbine Casing Models

Kazunari Fujiyama[*1]

Department of Mechanical Engineering, Meijo University/Faculty of Science and Technology
1-501 Shiogamaguchi Tempaku-ku, Nagoya 468-8502, Japan
[*1]fujiyama@meijo-u.ac.jp

Abstract- **The methodology was presented for evaluating creep-fatigue damage and for optimizing the shape of stress concentration in high temperature components under start-up cycles and steady state operations. Relatively simplified steam turbine casing models were employed by assigning shape parameters such as wall thickness t, fillet height t_s and fillet corner root radius R. Total 27 cases were investigated by FE(finite element) elastic thermal stress and pressure stress analysis for different sets of shape parameters. Elastic stress concentration factors were formulated by the shape parameters and by the reference plate stress under ramp temperature change for thermal stress and also by the internally pressurized cylinder stress under steady state conditions. Neuber's rule and cyclic stress-strain response were introduced and elastic-plastic strain ranges were obtained numerically. Fatigue life N_f was calculated by the material's low cycle fatigue properties for the elastic-plastic total strain range and creep rupture life t_r was calculated by the material's creep rupture properties for pressure stresses. The shape optimization was realized to set the corner radius as the object parameter by attaining the optimum sets of fatigue damage as the cycle fraction and creep damage as the time fraction to meet the non-linear creep-fatigue cumulative damage curve. This method was proved to be effective for shape optimization procedure even when non-linear material behaviours were exhibited.**

Keywords-Creep-fatigue; Damage; Thermal Stress; Stress Concentration; Steam Turbine; Casing; Shape Optimization

I. INTRODUCTION

Fossil power plants are still working as the primary energy sources currently all over the world. Steam turbines are the steam prime movers of steam power plants. Figure 1 shows the longitudinal cut view of high pressure steam turbine assembly which contains a high pressure rotor with buckets(moving blades), high pressure inner casings with nozzle boxes or nozzles and high pressure outer casings with main steam flanges. High temperature and high pressure conditions may cause severe creep and fatigue damage during operation and then outage after the long term service [1]. Therefore, it is indispensible to conduct the proper maintenance actions for the long term used components such as turbine casings which have complex geometries and large dimensions as shown in Fig.1, but it may require amounts of cost and time to make inspection and repair actions. Especially, the stress concentration geometries such as fillet corners could suffer from severe thermal fatigue conditions at start up cycles coupled with creep damage accumulation during steady operations. To reduce the accumulation of thermo-mechanical fatigue and creep combined damage (we abbreviate here as "creep-fatigue damage") [2] at these portions, shape optimization technique [3] is thought to be a useful tool. However, the design of casings may depend on the skills and experiences of design experts and the optimization methodology has not been fully established yet partly due to the complexity and non-linearity of the creep-fatigue damage phenomena. Therefore, this article aims to describe the current analytical shape optimization method using simplified models as an example of current status of solution under creep-fatigue conditions.

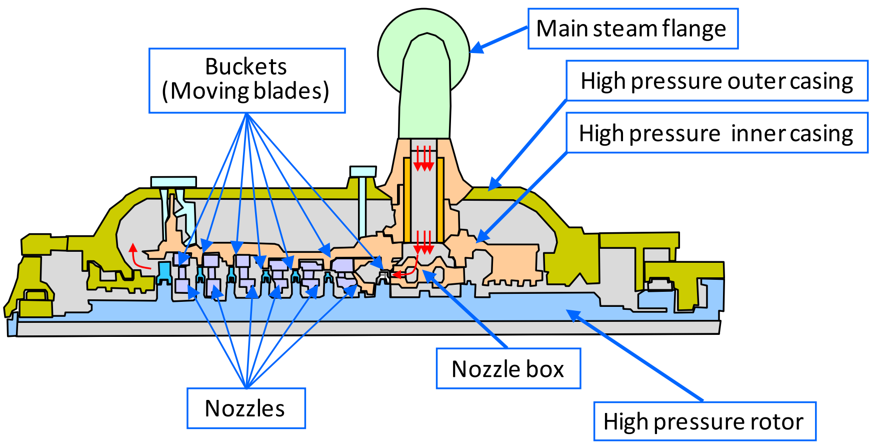

Fig. 1 xial cut view of a high pressure turbine assembly

II. CREEP-FATIGUE DESIGN APPROACH

Figure 2 shows the general flow-chart of creep-fatigue damage analysis and shape optimization. In this article, thermal stress analysis was conducted by elastic FEM and elastic-plastic stress-strain analysis was conducted through Neuber's rule[4] while the pressure stress analysis was conducted by elastic FEM. The full creep FE analysis was not adopted here because the steady state thermal stress might be compressive and relaxed rapidly and then the tensile pressure stress should become dominant in the relatively early stage of operation. Calculation of fatigue damage and creep damage was conducted independently by cycle fraction and time fraction using high temperature low cycle properties and creep rupture properties described later. Using creep-fatigue damage law as the design criteria, the optimization procedure was employed to find suitable corner root radius for the variety of other geometrical parameters.

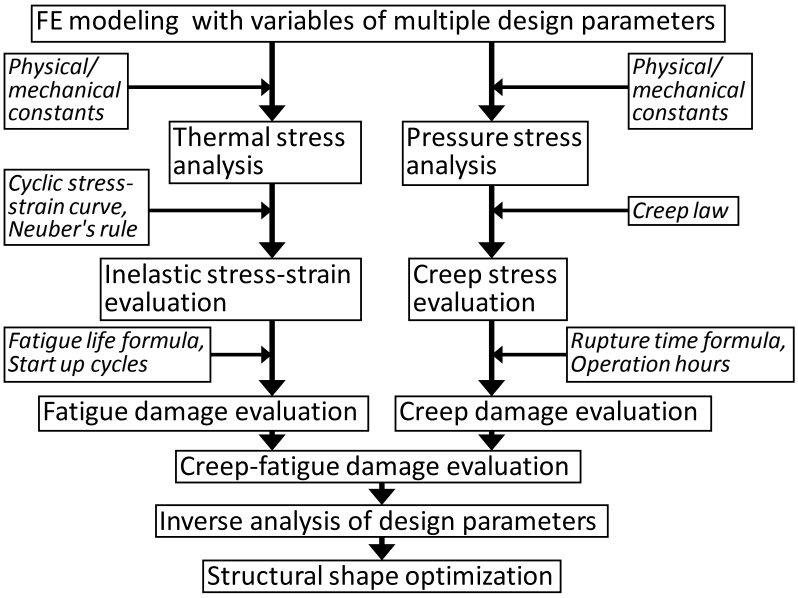

Fig. 2 The outline of optimum creep-fatigue design approach

III. FE MODELLING

A. FE Analysis Models

Figure 3 shows the FE modeling portion of casing as the axisymmetric cylinder including three fillets of the same configuration placed in the same intervals. FE calculations were conducted using the software MARC ver. 2005. Cracks would often emanate from the nozzle fit radius circumferentially due to the corner stress distribution. Figure 4 shows three models of cross sectional configuration for stress concentration calculation. (a) shows the original Gonyea's rotor model [5] without a bore hole, (b) shows the topologically identical model corresponding to the rotor model if it has a bore hole [6] and (c) shows the subject model we use here with three fillets to be more constrained than (b). In the original rotor case, Gonyea proposed the following formula for thermal stress concentration factor *TSCF* based on FE analysis following Peterson's mechanical stress concentration factor for shaft bending [7]. In this article, FE analysis based stress concentration factor was redefined using maximum thermal stress parameter concept for flat plate but Gonyea's formula was modified for creep stress concentration by FE pressure analysis conducted on model (c).

$$TSCF = 1 + \sqrt{\frac{D}{R}}\left(\frac{DEQ}{D} - 1\right)^{\frac{1}{\sqrt{2}}} \tag{1}$$

where,

$$\frac{DEQ}{D} = \min\left(\frac{D_1}{D}, 1 + 0.35\frac{L}{D}\right) \text{ for geometry shown in Fig.4(a)}$$

Table I shows the dimensional parameter sets for FE analyses. The dimensional variables are minimum wall thickness t, total height of fillet portion from outer surface t_s and nozzle fit corner radius R, while the fixed dimensions are total length A, fillet width L and inner diameter D_d, which result in total 27 cases. Figures 5 to 7 show all the FE mesh models used for all variations of t, t_s and R listed in Table I.

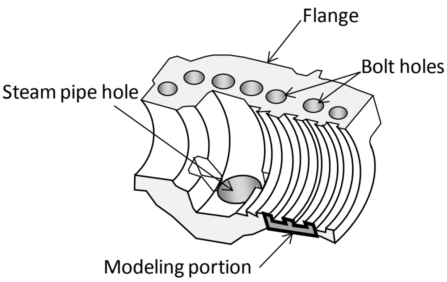

Fig. 3 Schematic of FE modelling portion

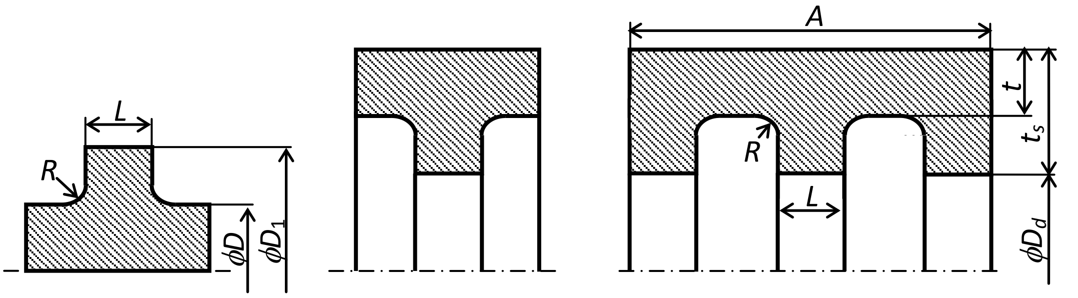

(a) Rotor (b) Casing 1 (c) Casing 2(current model)

Fig. 4 The comparison of simplified models for rotors and casings

TABLE I THE VARIATION IN THE DIMENSIONS OF CALCULATION MODEL

Dimensional symbol	Numerical values in mm								
t	50			100			150		
t_s	60			120			180		
	75			150			225		
	100			200			300		
R	1	5	10	2	10	20	3	15	30
A	600								
L	100								
D_d	500								

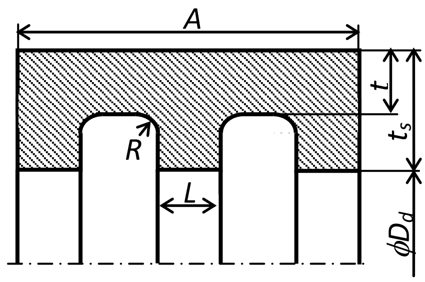

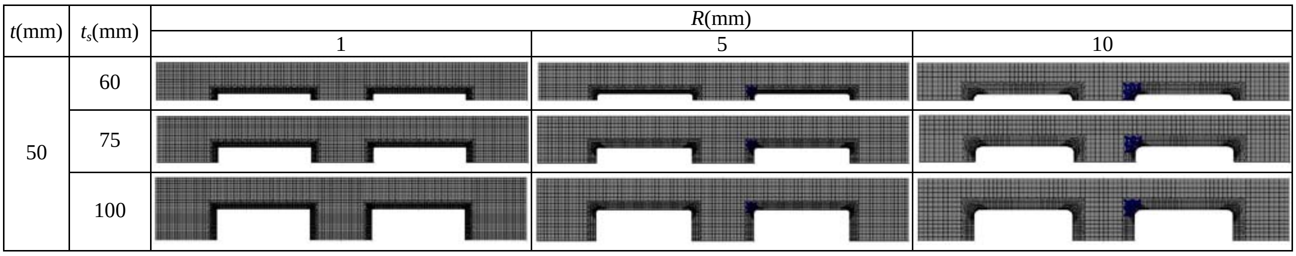

Fig. 5 FE mesh models in case of t=50mm

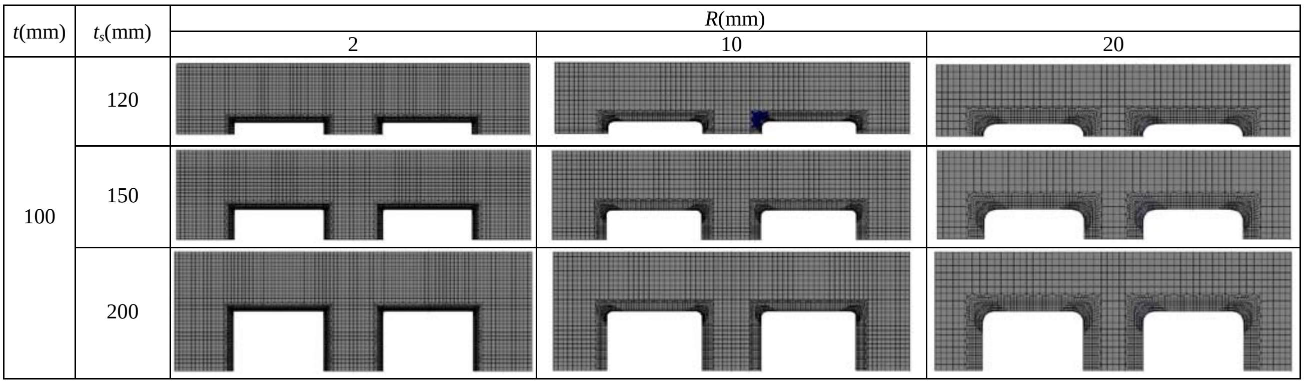

Fig. 6 FE mesh models in case of t=100mm

t(mm)	t_s(mm)	R(mm)		
		3	15	30
150	180	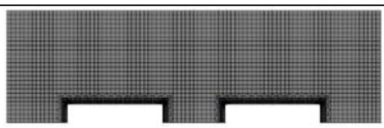	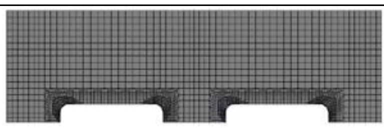	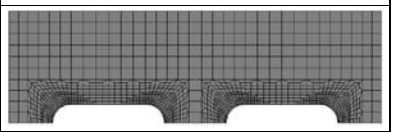
	225	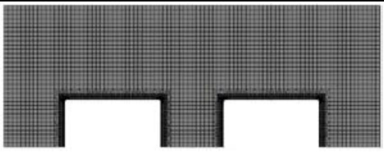	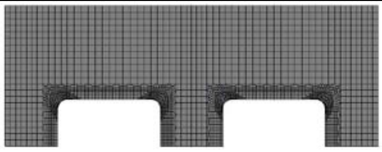	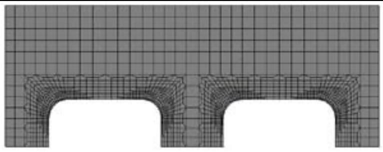
	300	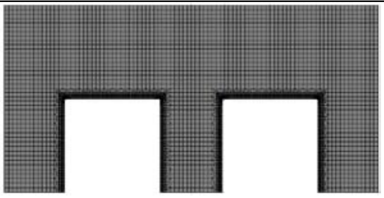	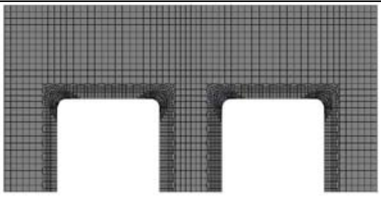	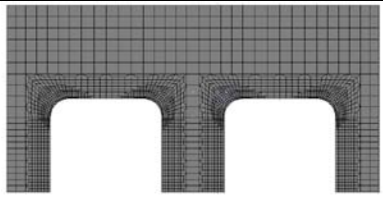

Fig. 7 FE mesh models in case of t=150mm

B. Boundary Conditions

Figure 8 shows the thermal boundary condition imposed area along the grooves between two adjacent fillets. Thermal conductivity was imposed for the edge film portion as a constant value of 11630W/(m^2·K). This value (corresponding to 10^{4}kcal/m^2/h/°C) was adopted as the typical upper case for the inlet steam condition of high pressure turbine. Figure 9 shows the pressure boundary condition imposed area for creep stress calculation. Figure 10 shows the steam temperature trend for FE calculation. This temperature trend was imposed on the boundary condition areas.

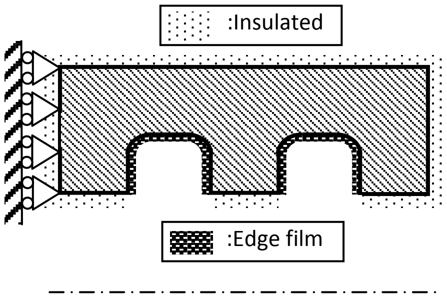

Fig. 8 Area of boundary conditions for thermal analysis

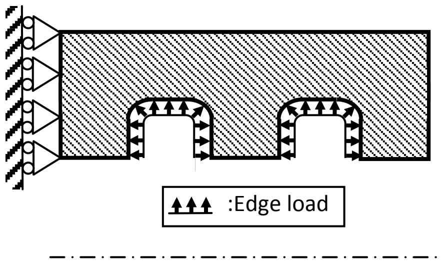

Fig. 9 Area of boundary conditions for pressure stress analysis

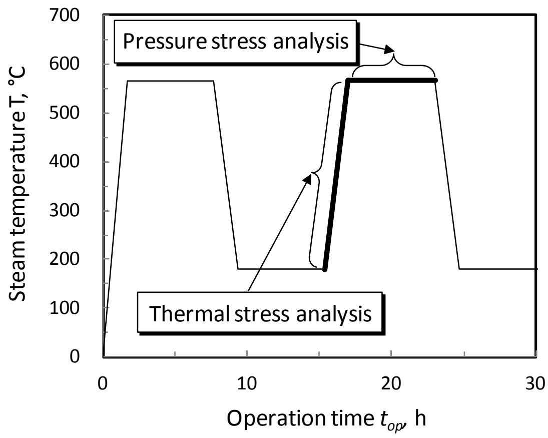

Fig. 10 Steam temperature change for FE calculation

C. Physical Properties for Thermal Analysis

Figures 11 and 12 show the temperature dependence of specific heat [8] and thermal conductivity [8] of subject material which were used in the calculation of temperature distribution. Regression curves are derived from the regression of the plotted data by the second order polynomials as indicated in these figures. As the temperature dependence of specific heat could not be obtained for 1Cr1Mo0.25V cast, 2.25Cr1.6WVNb steel data were utilized instead as the only available data at present.

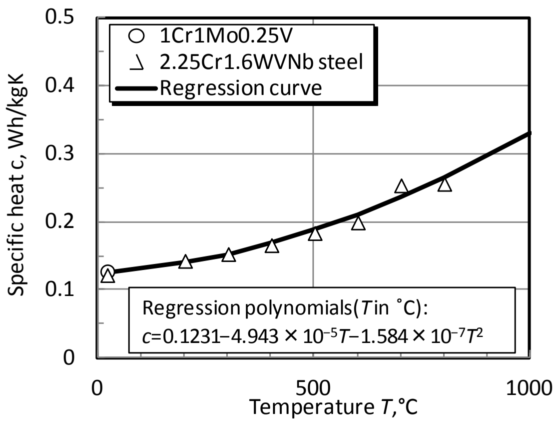

Fig. 11 Temperature dependence of specific heat.

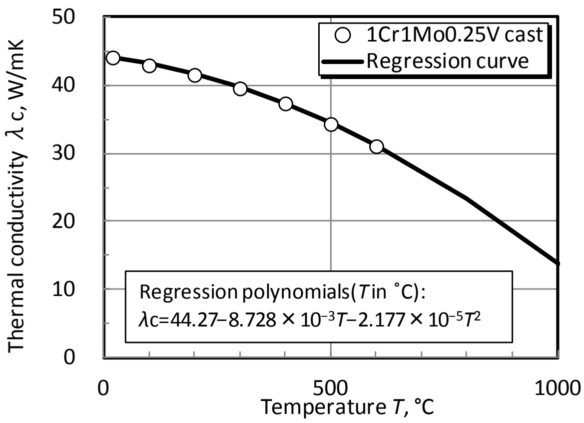

Fig.12 Temperature dependence of thermal conductivity.

IV. FE ANALYSIS RESULTS

A. Thermal Stress Distribution

Table II shows the FE calculation results. In this table, σ_{lFEM} means local peak thermal stress at the corner of radius, σ_{nFEM} means the corresponding thermal stress at the flat portion (i.e. surface stress at mid -position between two fillets) and σ_{pFEM} means pressure stress. All stress values are expressed as von Mises equivalent stresses hereafter. Elastic stress concentration factor K_{tFEM} is defined as the ratio of σ_{lFEM} to σ_{nFEM} .

Figures 13 to 15 show the von MISES equivalent thermal stress maps for each configuration. The pressure stress maps will be shown later. Unfortunately, the stress contour scaling is different among each case, the upper and lower stress levels as well as the stress intervals are noted in each column for the convenience of reference. It can be found that stress localization is more apparent for smaller fillet corner root radius. This stress distribution suggests that the start-up thermal stress damage is highly localized in the fillet corner root positions. The flat portion stress is obtained from the flat portion apart from the fillet corner root stress concentration.

TABLE II RESULT OF FE ANALYSIS

t(mm)	t_s(mm)	R(mm)	Thermal stress			Pressure stress
			σ_{lFEM}(MPa)	σ_{nFEM}(MPa)	K_{tFEM}	σ_{pFEM}(MPa)
50	60	1	469.96	151.67	3.10	189.32
		5	255.27	147.05	1.74	191.28
		10	199.96	136.75	1.46	193.56
	75	1	591.42	154.10	3.84	247.62
		5	302.05	145.85	2.07	171.66
		10	225.64	136.89	1.65	173.90
	100	1	681.48	154.78	4.40	317.02
		5	329.74	146.08	2.26	179.10
		10	240.38	136.27	1.76	154.52
100	120	2	1066.47	304.27	3.51	116.75
		10	576.00	293.77	1.96	88.75
		20	440.99	277.46	1.59	90.19
	150	2	1225.70	275.99	4.44	156.43
		10	622.27	261.26	2.38	94.48
		20	458.47	242.62	1.89	86.01
	200	2	1298.36	251.28	5.17	225.66
		10	637.89	233.71	2.73	120.33
		20	459.84	214.52	2.14	100.74
150	180	3	1464.17	444.13	3.30	111.41
		15	831.43	440.15	1.89	70.67
		30	681.05	435.34	1.56	69.31
	225	3	1570.85	392.51	4.00	152.65
		15	841.49	383.44	2.19	85.14
		30	671.56	377.40	1.78	78.14
	300	3	1650.63	342.68	4.82	238.44
		15	842.92	328.20	2.57	131.90
		30	653.45	321.64	2.03	116.45

t(mm)	t_s(mm)	R(mm)		
		1	5	10
50	60	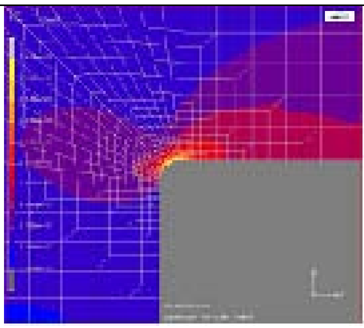 Upper:267.4 MPa Lower:7.635 MPa Interval:26 MPa	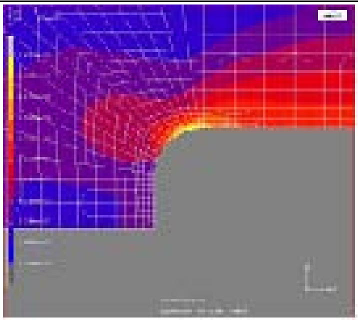 Upper:145.2 MPa Lower:5.566 MPa Interval:14 MPa	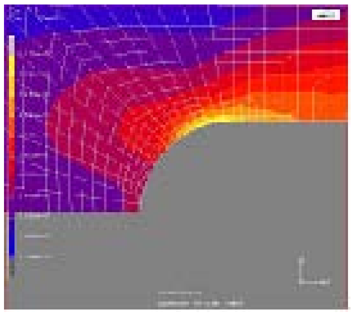 Upper:113.7 MPa Lower:2.983 MPa Interval:11.1 MPa
	75	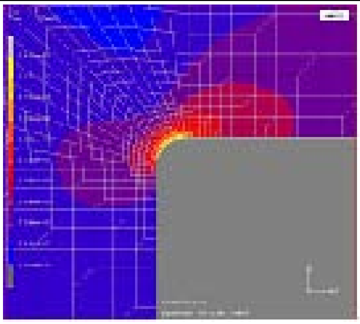 Upper:341.1MPa Lower:2.836MPa Interval:33.8MPa	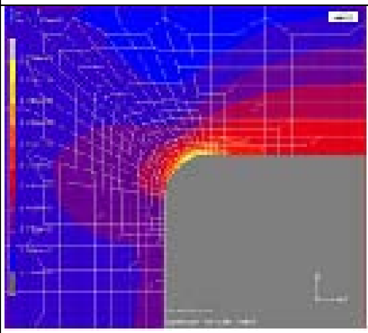 Upper:171.5MPa Lower:3.987MPa Interval:16.7MPa	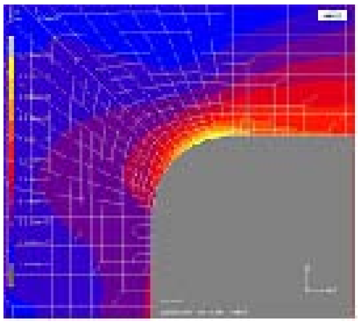 Upper:128.1MPa Lower:7.426MPa Interval:12.1MPa
	100	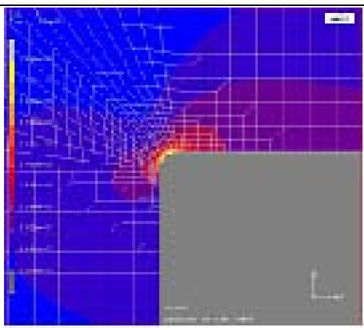 Upper:386.9MPa Lower:3.638MPa Interval:38.3MPa	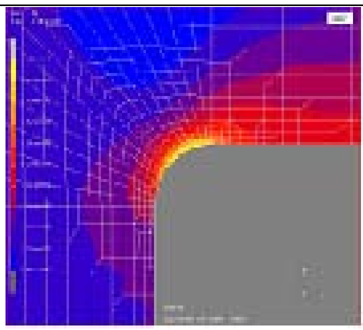 Upper:187.1MPa Lower:4.752MPa Interval:18.2MPa	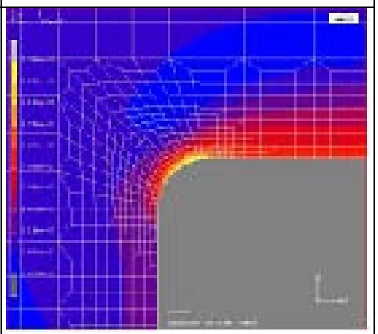 Upper:136.3MPa Lower:5.47MPa Interval:13.1MPa

Fig. 13 Equivalent thermal stress maps by FE calculation in case of t=50mm

t(mm)	t_s(mm)	R(mm)		
		2	10	20
100	120	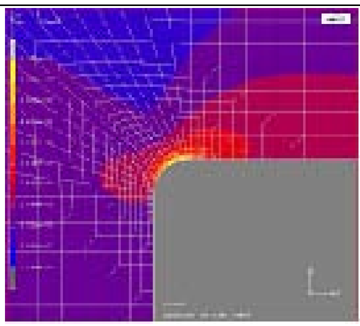 Upper:630.4MPa Lower:7.766MPa Interval:62.3MPa	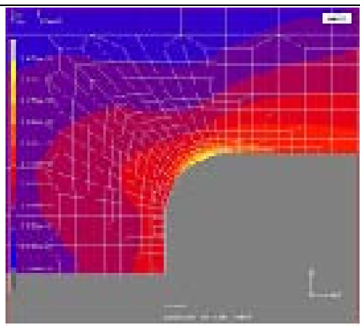 Upper:347.6MPa Lower:7.513MPa Interval:34.0MPa	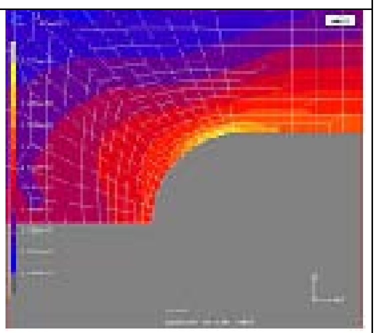 Upper:272.2MPa Lower:11.03MPa Interval:26.1MPa

	150	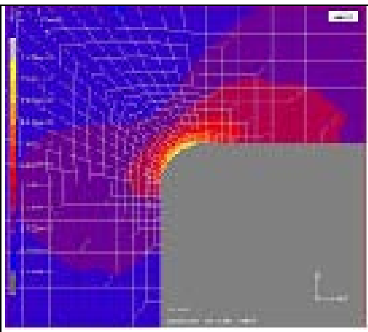 Upper:727.4MPa Lower:8.215MPa Interval:71.9MPa	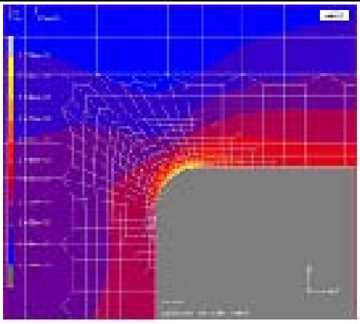 Upper:377.4MPa Lower:11.34MPa Interval:36.6MPa	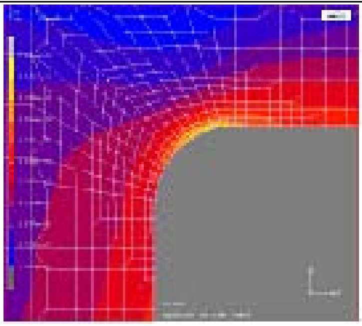 Upper:286.6MPa Lower:9.675MPa Interval:27.7MPa
	200	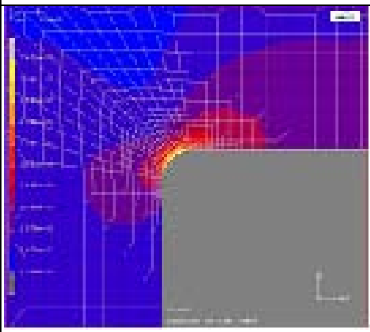 Upper:767.5MPa Lower:5.52MPa Interval:76.2MPa	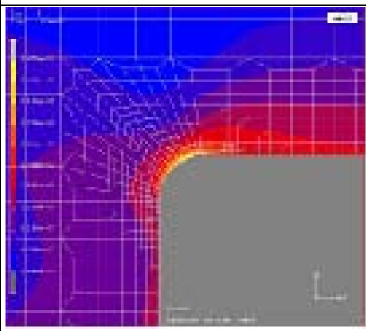 Upper:387.3MPa Lower:5.443MPa Interval:38.2MPa	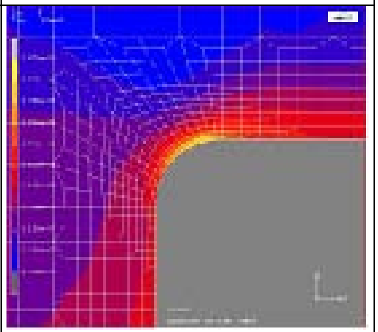 Upper:287.6MPa Lower:4.383MPa Interval:28.3MPa

Fig. 14 Equivalent thermal stress maps by FE calculation in case of t=100mm

t(mm)	t_s(mm)	R(mm)		
		3	15	30
150	180	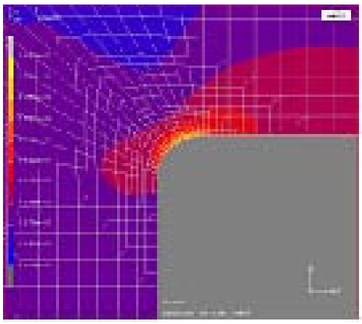 Upper:1001MPa Lower:21.55MPa Interval:97.9MPa	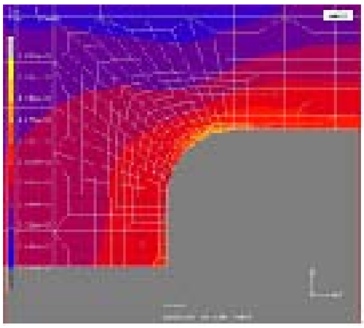 Upper:589.2MPa Lower:17.39MPa Interval:57.2MPa	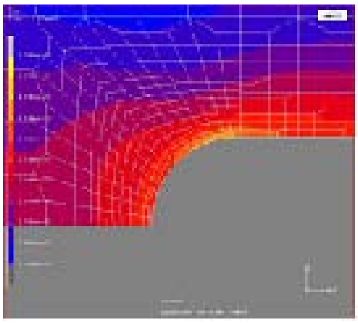 Upper:508.3MPa Lower:8.522MPa Interval:50.0MPa
	225	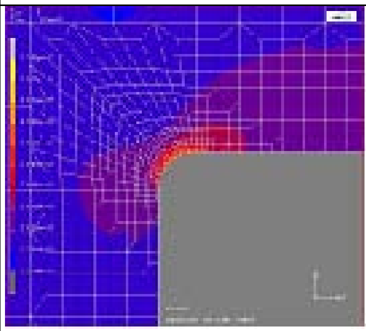 Upper:1281MPa Lower:7.798MPa Interval:127.3MPa	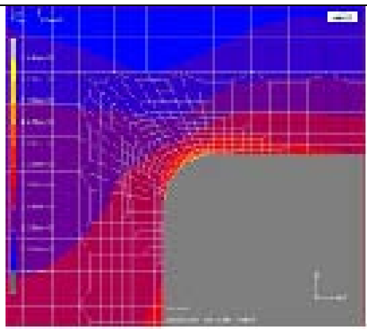 Upeer:664.5MPa Lower:7.410MPa Interval:65.7MPa	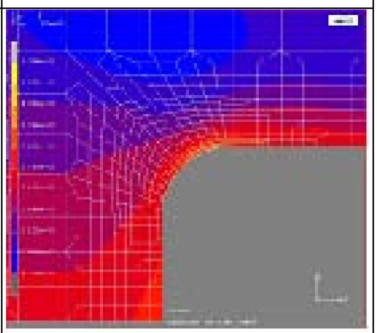 Upper:536.4MPa Lower:4.936MPa Interval:53.2MPa

	300	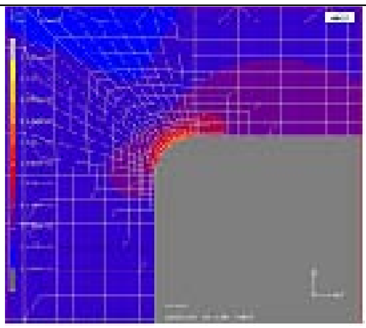 Upper:1371MPa Lower:5.682MPa Interval:136.6MPa	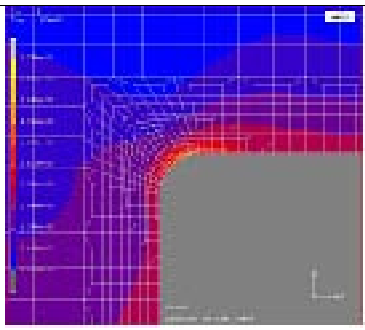 Upper:679.4MPa Lower:3.832MPa Interval:67.6MPa	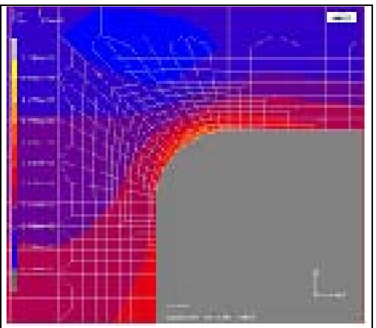 Upper:534.1MPa Lower:0MPa Interval:53.5MPa

Fig. 15 Equivalent thermal stress maps by FE calculation in case of t=150mm

B. Evaluation of Inelastic Stress Strain Concentration

To evaluate thermal fatigue damage, local inelastic stress strain values should be evaluated. In this article, the formula of thermal stress concentration will be established as the function of geometrical parameters and the basic plate thermal stresses. To evaluate the reference plate thermal stress σ_{plate} defined as the maximum thermal stress of flat plate subjected to ramp change of temperature with time on one side surface and insulated on the other side, the maximum thermal stress parameter CSH_{max}[9] is introduced as the indicator of the intensity of thermal stress level defined as follows if we assume the plane strain condition.

$$CSH_{\max} \equiv \frac{\sigma_{plate} \cdot (1-\nu)}{\alpha E \Delta T_f} \tag{2}$$

Where, α: coefficient of linear expansion (1/K), E:Young's modulus(MPa), ν:Poisson's ratio(here, put as 0.3), ΔT_f: the range of fluid temperature change(K)

For regression analysis of CSH_{max} curves, the logistic curve function[10] form was utilized as follows.

$$CSH_{\max} = \frac{0.03A\exp(At')}{A-0.03B\{1-\exp(At')\}} \tag{3}$$

where, $t' = 1-\log(t_L^*)$, $t_L^* = a\dfrac{t_L}{L^2}$, t_L: ramp time(s), L:Plate thickness(m), $a = \dfrac{\lambda}{c\rho}$:Thermal diffusivity(m^2/s), λ:Thermal conductivity(W/mK), c:Specific heat(Ws/kgK), ρ:Mass density(kg/m^3)

$$A_T = 10^{\left\{\sum_{i=0}^{4} A_{Ti}(\log Bio)^i\right\}}, \quad B_T = 10^{\left\{\sum_{i=0}^{4} B_{Ti}(\log Bio)^i\right\}}$$ *,ATi, BTi(i=0,4): Regression constants*

The resultant curves are shown in Fig.16. Then the reference plate thermal stress σ_{plate} is calculated by CSH_{max}.from Eq.(2) as follows.

$$\sigma_{plate} = \frac{CSH_{\max} \cdot \alpha E \Delta T_f}{1-\nu} \tag{4}$$

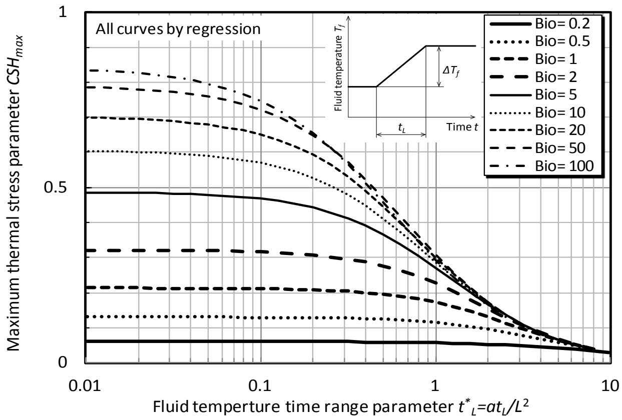

Fig. 16 Diagram for evaluation of maximum thermal stress parameter CSH_{max}

As the local stress at corner by FEM σ_{lFEM} showed apparent dependence of corner radius R as shown in Figs.17 and 18, we can get the following expression by regression. The estimated flat portion stress is denoted as σ_{les}.

$$\sigma_{les} = b_l R^{\beta_l} \sigma_{plate}^{\alpha_l} \tag{5}$$

where, σ_{les}: estimated local thermal stress by Eq.(5), α_l, β_l, b_l : constants.

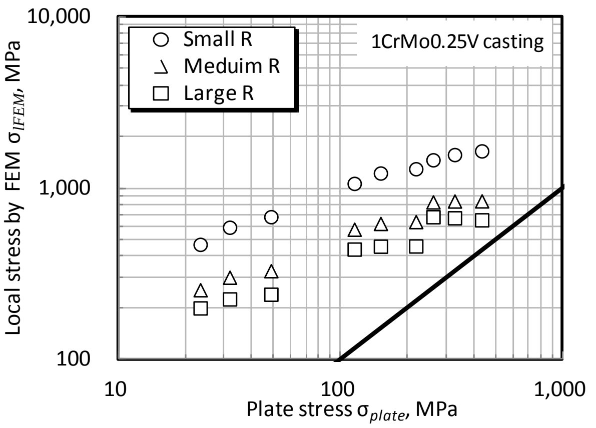

Fig. 17 Relationship between plate stress and local stress by FEM

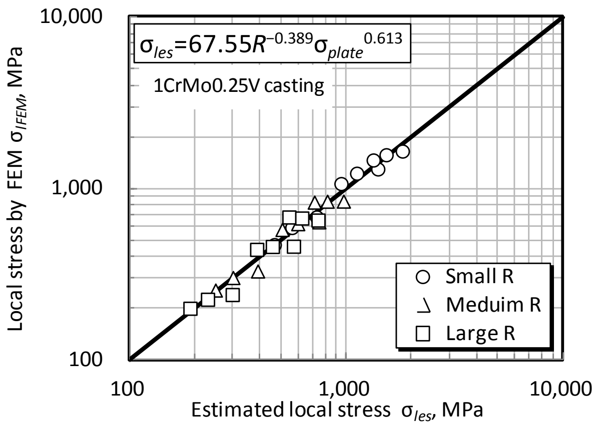

Fig.18 Comparison of estimated local stress by formula and local stress by FEM

For flat portion stress by FEM σ_{nFEM} can be expressed by the following equation as the function of the reference plate thermal stress σ_{plate}, corner radius R, thicknesses t and t_s as shown in Figs.19 and 20. The estimated flat portion stress is denoted as σ_{nes}.

$$\sigma_{nes} = b_{fl} \left(t + t_s\right)^{\gamma_{fl}} R^{\beta_{fl}} \sigma_{plate}^{\alpha_{fl}} \tag{6}$$

where, α_l, β_l, b_l : constants.

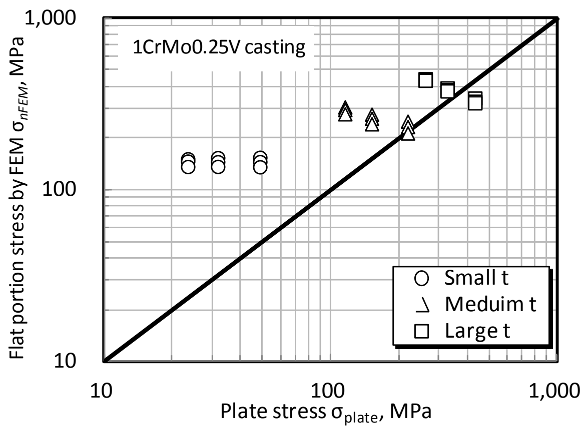

Fig. 19 Relationship between plate stress and flat portion stress by FEM

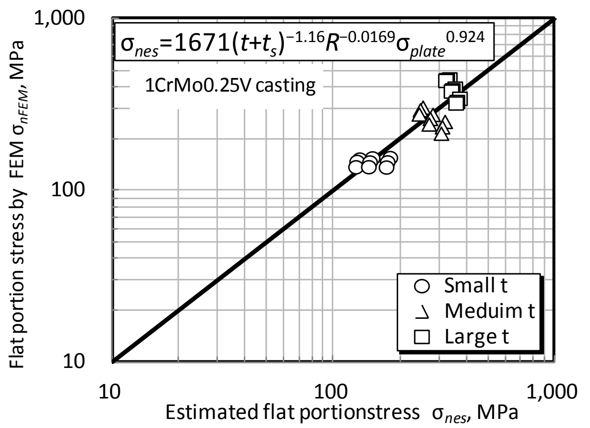

Fig.20 Comparison of estimated flat portion stress by formula and by FEM

Even in the flat portion stress of FE analysis, the influence of the stress distribution at fillet corner root radius is still observed. Therefore, the stress concentration factor by FE analysis K_{tFEM} should be defined as the ratio of the local FEM von Mises equivalent stress to the flat portion FEM von Mises equivalent stress as indicated in Eq.(7). While we can also obtain the estimated thermal stress concentration factor K_{tes} as Eq.(8) by the ratio of Eq.(5) to Eq.(6) as the approximation of K_{tFEM}. The estimated K_{tes} and actual K_{tFEM} showed good coincidence as shown in Fig.21.

$$K_{tFEM} = \frac{\sigma_{lFEM}}{\sigma_{nFEM}} \tag{7}$$

$$K_{tes} = \frac{\sigma_{les}}{\sigma_{nes}} = b_t \left(t + t_s\right)^{\gamma_t} R^{\beta_t} \sigma_{plate}^{\alpha_t} \tag{8}$$

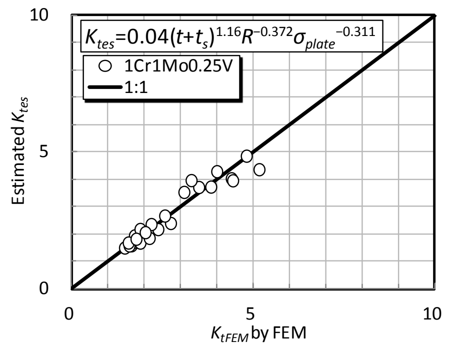

Fig. 21 Comparison of stress concentration factor Kt calculated by FEM and estimated by formula

From Neuber's rule [4], we can get the relationship between local stress range $\Delta\sigma_{ep}$ and strain range $\Delta\varepsilon_t$ by Eq.(9). The number of 100 is used in case of strains in %. Moreover, we can solve the local total strain range $\Delta\varepsilon_t$ combining Eq.(10) and Fig.22 with material's cyclic stress-strain response expressed by Eq.(11) as the summation of elastic part and plastic part. The plastic part is determined by the regression analysis from room temperature to 600˚C(873K) as shown in Fig.22.

$$K_\sigma K_\varepsilon = \frac{\Delta\sigma_{ep}}{\Delta\sigma_{nes}}\frac{\Delta\varepsilon_t}{\Delta\varepsilon_{nes}} = \frac{\Delta\sigma_{ep}}{\Delta\sigma_{nes}}\frac{E\Delta\varepsilon_t}{100\Delta\sigma_{nes}} = K_t^2 = \left(\frac{\Delta\sigma_{les}}{\Delta\sigma_{nes}}\right)^2 \tag{9}$$

$$\therefore \Delta\sigma_{ep} = \frac{100\Delta\sigma_{les}^2}{E\Delta\varepsilon_t} \tag{10}$$

$$\Delta\varepsilon_t = \frac{100\Delta\sigma_{ep}}{E} + \left(\frac{\Delta\sigma_{ep}}{A_p\sigma_B}\right)^{\frac{1}{n_p}} \tag{11}$$

where, K_σ: elastic-plastic (or actual) stress concentration factor(=$\Delta\sigma_{ep}/\Delta\sigma_{nes}$) , Kε: elastic-plastic (or actual) strain concentration factor (=$\Delta\sigma_{ep}/\Delta\sigma_{nes}$) , $\Delta\sigma_{nes}$: nominal stress range(MPa), $\Delta\varepsilon_{nes}$: nominal strain range (=$\Delta\sigma_{nes}/E\times100$, %), K_t: nominal stress concentration factor, $\Delta\sigma_{les}$: local elastic stress range(MPa), σ_B: tensile strength at subject temperature(MPa), A_p, n_p: material constants as shown in Fig.22.

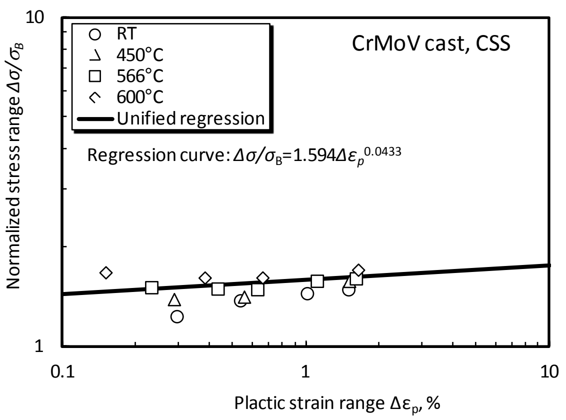

Fig. 22 Unified cyclic stress range - plastic strain range relationship for subject material

Eq.(12) is the modification of Eq.(11) substituted by Eq.(10) for solving the local total strain range $\Delta\varepsilon_t$. As this equation cannot be solved explicitly, we must search the numerical solution. The solution can be indicated in Fig.23 as the intersection of Eq.(10) and Eq.(11). Stress range values are obtained by multiplying 2 to the stress amplitude values because if the thermal stress at start up is fully relieved by stress relaxation during steady state operation, the shut down thermal stress can be up to the stress level of start-up. This assumption is considerably safer side estimation but often used for life assessment of actual components [12].

$$\Delta\varepsilon_t^2 - \left(\frac{100\Delta\sigma_{nes}^2 K_t^2}{EA_p\sigma_B}\right)^{\frac{1}{n_p}} \Delta\varepsilon_t^{\,1-\frac{1}{n_p}} - \frac{10000\Delta\sigma_{nes}^2 K_t^2}{E^2} = 0 \tag{12}$$

where,

$$\Delta\sigma_{nes} = 2b_{fl}\left(t+t_s\right)^{\gamma_{fl}} R^{\beta_{fl}} \sigma_{plate}^{\alpha_{fl}} \tag{13}$$

or

$$\Delta\varepsilon_t^2 - \left(\frac{100\Delta\sigma_{les}^2}{EA_p\sigma_B}\right)^{\frac{1}{n_p}} \Delta\varepsilon_t^{1-\frac{1}{n_p}} - \frac{10000\Delta\sigma_{les}^2}{E^2} = 0 \tag{14}$$

where,

$$\Delta\sigma_{les} = 2b_l R^{\beta_l} \sigma_{plate}^{\alpha_l} \tag{15}$$

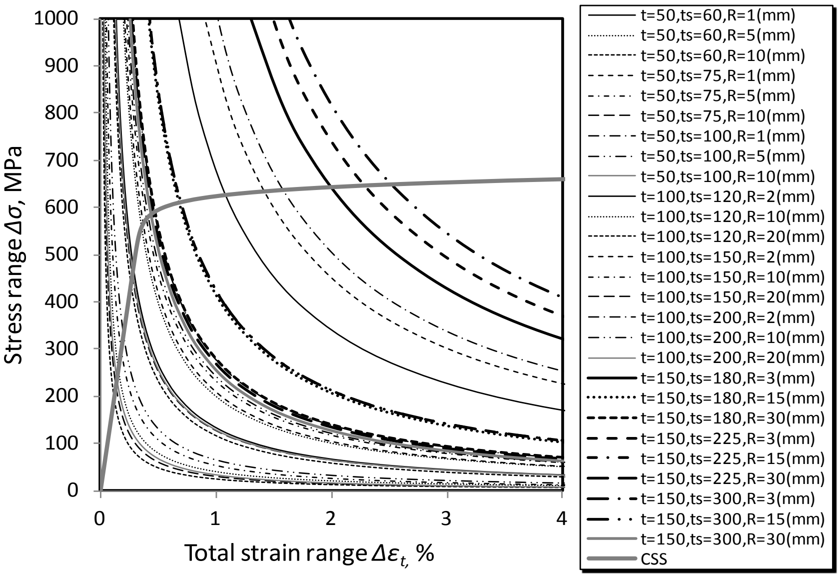

Fig. 23 Elastic-plastic stress strain determination using Neuber's rule and cyclic stress-strain curve

TABLE III LOCAL STRAIN RANGE AND STRESS RANGE OBTAINED BY NEUBER'S RULE

t(mm)	t_s(mm)	R(mm)	Total strain range $\Delta\varepsilon_t$(%)	Elastic-plastic stress range $\Delta\sigma_{ep}$ (MPa)
50	60	1	0.8560	619.3
		5	0.3069	509.6
		10	0.2400	399.9
	75	1	1.3269	632.7
		5	0.3830	571.8
		10	0.2708	451.3
	100	1	1.7415	640.1
		5	0.4444	587.3
		10	0.2886	480.6
100	120	2	4.1293	661.1
		10	1.2614	631.3
		20	0.7590	615.0
	150	2	5.4035	667.4
		10	1.4627	635.4
		20	0.8168	617.7
	200	2	6.0400	669.9
		10	1.5340	636.7
		20	0.8214	617.9
150	180	3	7.6208	675.2
		15	2.5539	649.7
		30	1.7394	640.0
	225	3	8.7318	678.3
		15	2.6138	650.3
		30	1.6932	639.3
	300	3	9.6104	680.5
		15	2.6224	650.3
		30	1.6065	638.0

C. Pressure Stress Analysis

Figures 24 to 26 show the FE analysis results. For shallow notch type fillets, the maximum stress portion moved to the flat surface portion, while for deep notch type fillets, the pressure stress concentrated at the corner radius. The strong sensitivity of corner root radius was also observed and the stress distribution features suggested that the effect of bending moment from the fillet area was significant. In Fig.24, the small value of wall thickness t and the low height of t_s resulted in the flat portion inner surface between fillets. Other cases showed that stress concentration was located at the fillet corner root radius. In this study, von MISES equivalent pressure stresses are adopted as the values at the same position of the maximum thermal stress at start-up stage for evaluating creep-fatigue damage analysis.

t(mm)	t_s(mm)	R(mm)		
		1	5	10
50	60	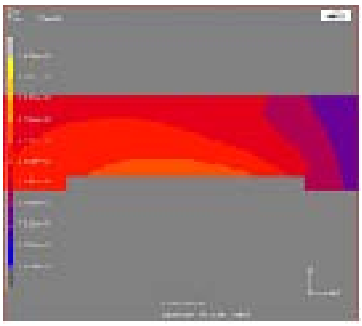 Upper:263.9MPa Lower:22.91MPa Interval:24.1MPa	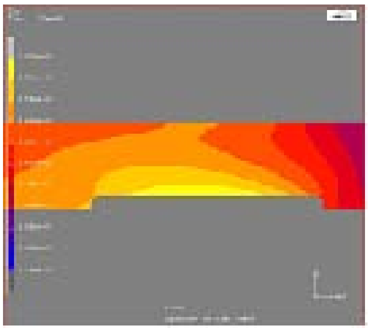 Upper:191.3MPa Lower:27.21MPa Interval:16.4MPa	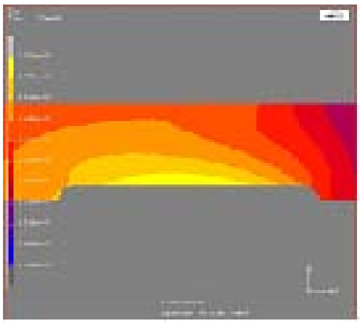 Upper:193.6MPa Lower:33.03MPa Interval:16.1MPa
	75	 Upper:453.8MPa Lower:26.11MPa Interval:42.8MPa	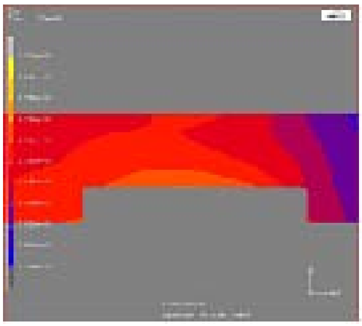 Upper:231.1MPa Lower:29.94MPa Interval:20.1MPa	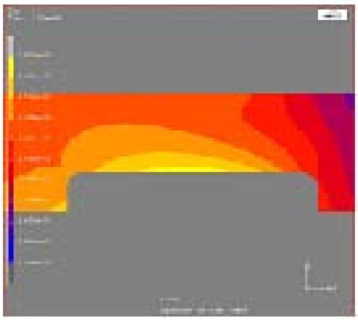 Upper:181.2MPa Lower:35.16MPa Interval:14.6MPa
	100	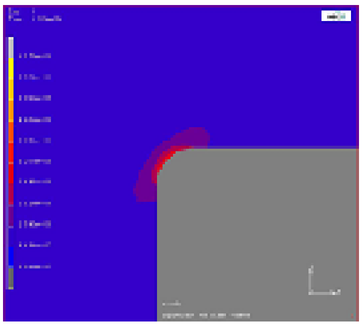 Upper:617.3MPa Lower:38.11MPa Interval:57.9MPa	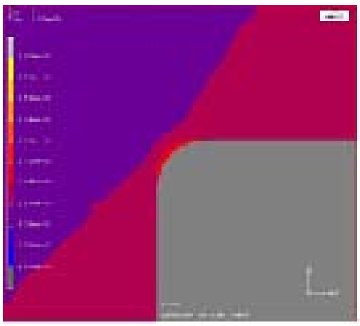 Upper:302.4MPa Lower:41.5MPa Interval:26.1MPa	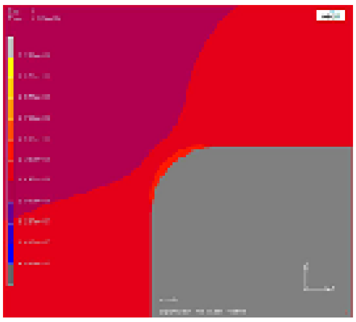 Upper:225.8MPa Lower:46.13MPa Interval:18.0MPa

Fig. 24 Equivalent pressure stress maps by FE calculation in case of t=50mm

t(mm)	t_s(mm)	R(mm)		
		2	10	20
100	120	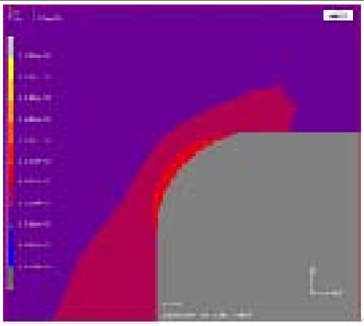 Upper:198.0MPa Lower:32.52MPa Interval:16.5MPa	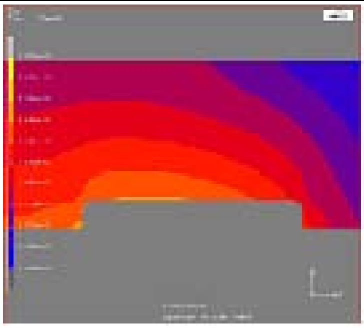 Upper:107.3MPa Lower:36.56MPa Interval:7.07MPa	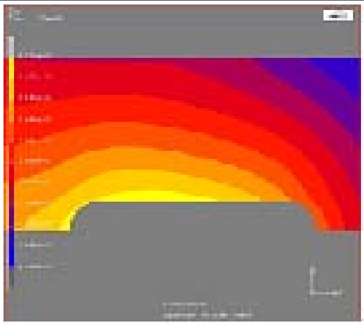 Upper:91.75MPa Lower:42.01MPa Interval:4.97MPa
	150	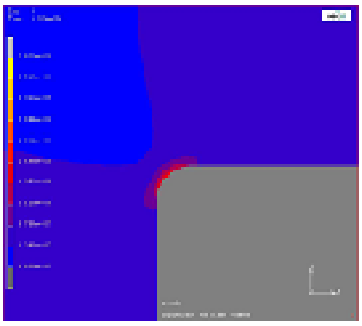 Upper:281.1MPa Lower:38.58MPa Interval:24.2MPa	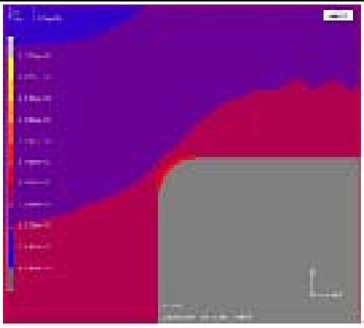 Upper:137.2MPa Lower:42.42MPa Interval:9.5MPa	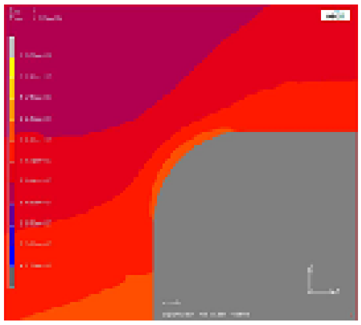 Upper:103.8MPa Lower:47.72MPa Interval:5.6MPa
	200	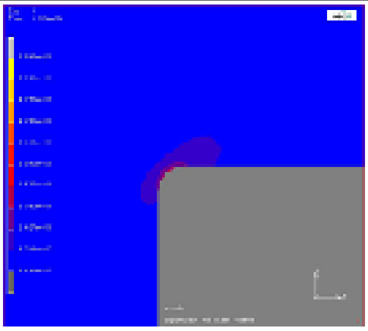 Upper:586.8MPa Lower:31.68MPa Interval:55.5MPa	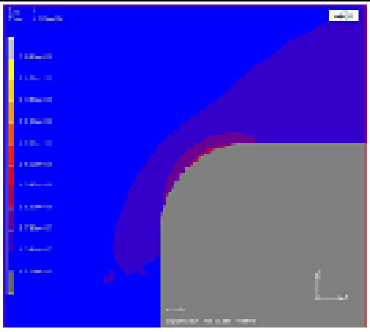 Upper:288.5MPa Lower:37.73MPa Interval:25.1MPa	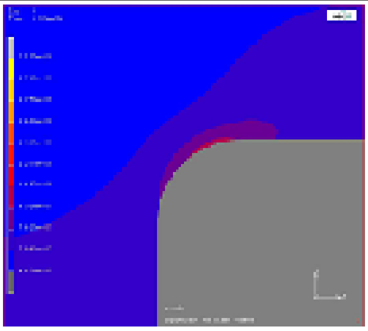 Upper:213.7MPa Lower:41.71MPa Interval:17.2MPa

Fig. 25 Equivalent pressure stress maps by FE calculation in case of t=100mm

t(mm)	t_s(mm)	R(mm)		
		3	15	30
150	180	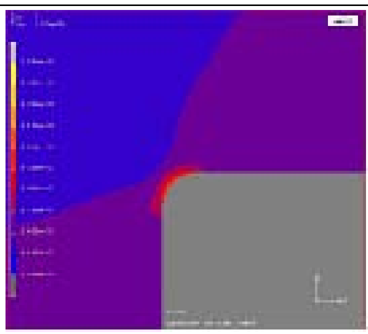 Upper:158.1MPa Lower:28.08MPa Interval:13MPa	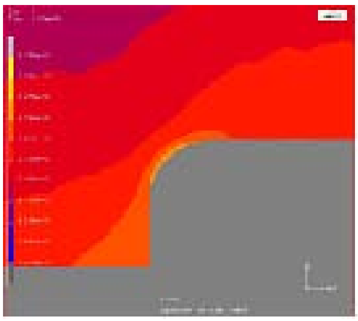 Upper:82.97MPa Lower:31.73MPa Interval:5.12MPa	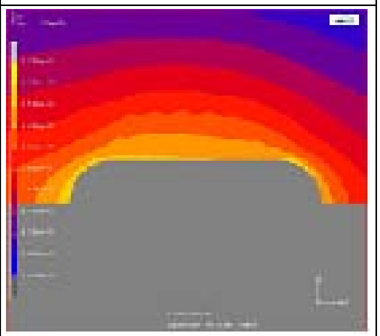 Upper:72.92MPa Lower:36.7MPa Interval:3.62MPa

	225	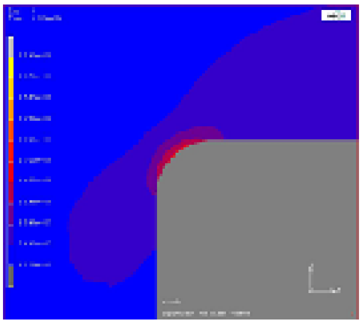 Upper:316.5Mpa Lower:27.75MPa Interval:28.9MPa	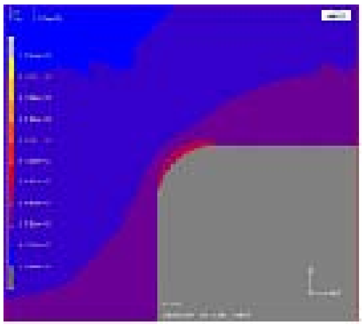 Upper:156.6MPa Lower:30.64MPa Interval:12.6MPa	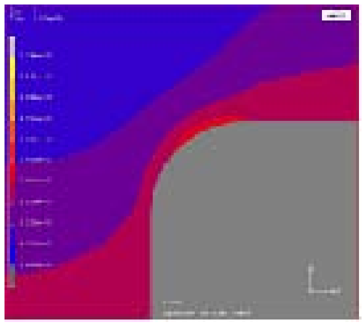 Upper:124.4MPa Lower:34.25MPa Interval:9MPa
	300	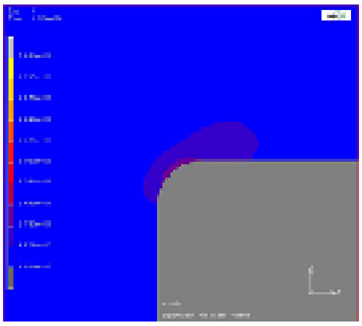 Upper:769.6MPa Lower:20.36MPa Interval:74.9MPa	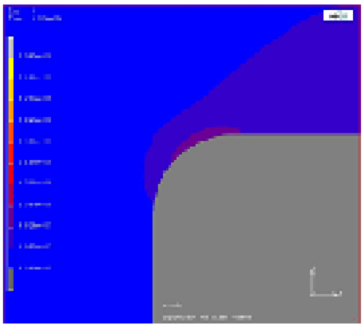 Upper:398.7MPa Lower:23.0MPa Interval:37.6MPa	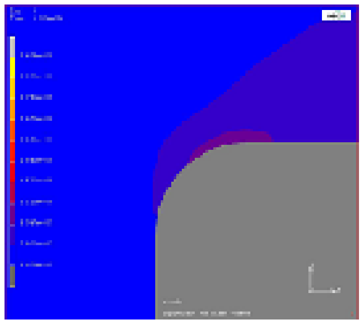 Upper:341.4MPa Lower:25.73MPa Interval:31.5MPa

Fig. 26 Equivalent pressure stress maps by FE calculation in case of *t*=150mm

D. Evaluation of Pressure Stress Concentration at Corner Root Radius

To express the stress concentration for pressure stress analysis, the creep stress concentration factor $K_{\sigma crp}$ was also defined here as the ratio of corner root radius stress to long hollow cylinder pressure stress though in some cases it was found that the higher stresses were distributed along flat area than corner root radius. The equivalent stress of long smooth cylinder for steady creep state can be expressed by the following equations. It follows the Gonyea's original expression [5] by Eq.(1).

$$K_{\sigma crp} = \frac{\sigma_{c,FEM}}{\sigma_{eq,cylinder}} = 1 + 0.126\left(\frac{t}{R}\right)^{0.59}\left(\frac{t_{EQ}}{t} - 1\right)^{0.148} \tag{16}$$

$$\sigma_{eq,cylinder} = \sqrt{\frac{1}{2}\left\{(\sigma_\theta - \sigma_r)^2 + (\sigma_r - \sigma_z)^2 + (\sigma_z - \sigma_\theta)^2\right\}} = \frac{\sqrt{3}p\left(\frac{r_o}{r}\right)^{\frac{2}{\alpha_c}}}{\left(\frac{r_o}{r_i}\right)^{\frac{2}{\alpha_c}} - 1} \tag{17}$$

where, α_c is the creep exponent when minimum creep rate $\dot{\varepsilon}_m$ is expressed by the following Norton's law [4] and takes the value of 13.686 here.

$$\dot{\varepsilon}_m = B_0\left(\frac{\sigma_{eq}}{HV}\right)^{\alpha_c}\exp\left(-\frac{Q_c}{n_m kT}\right), \tag{18}$$

B_0:constant(it takes the value of 5.51×10^{20} here), σ_{eq}: von Mises equivalent stress(MPa), HV: Vickers hardness, Qc: activation energy for minimum creep rate(kJ/mol)[12], k: Boltzmann constant(=1.38×10^{-23}J/K), n_m: mol number(=6.025×10^{23}), T:temperature(K). Eq.(18) was determined from data regression of subject material as shown in Fig.27.

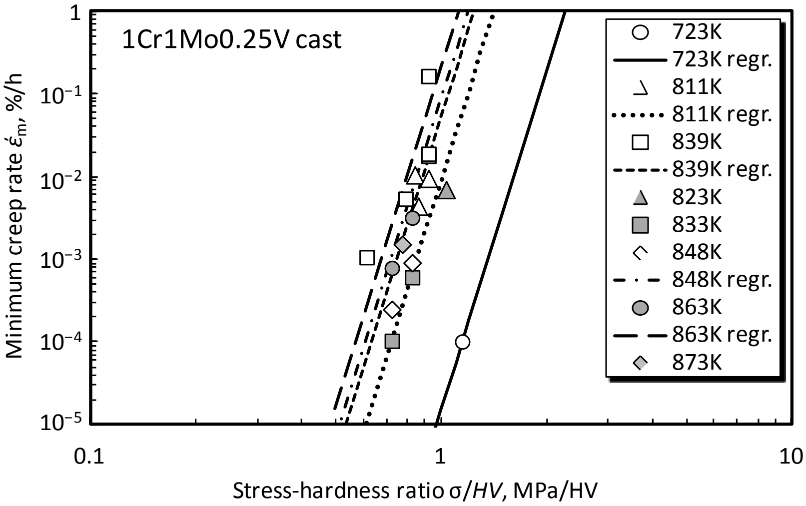

Fig.27 Relationship between minimum creep rate and stress-hardness ratio for 1Cr1Mo0.25V cast steel

Moreover, the stress components in Eq.(17) were expressed as the following forms;

$$\sigma_\theta = p\frac{\left(\frac{2}{\alpha}-1\right)\left(\frac{r_o}{r}\right)^{\frac{2}{\alpha}}+1}{\left(\frac{r_o}{r_i}\right)^{\frac{2}{\alpha}}-1}, \quad \sigma_r = -p\frac{\left(\frac{r_o}{r}\right)^{\frac{2}{\alpha}}-1}{\left(\frac{r_o}{r_i}\right)^{\frac{2}{\alpha}}-1}, \quad \sigma_z = p\frac{\left(\frac{1}{\alpha}-1\right)\left(\frac{r_o}{r}\right)^{\frac{2}{\alpha}}+1}{\left(\frac{r_o}{r_i}\right)^{\frac{2}{\alpha}}-1},$$

$$r_i = \frac{D_d}{2}+t_s-t, \quad r_o = \frac{D_d}{2}+t_s$$

R: corner root radius, $\frac{t_{EQ}}{t} = \max\left(\frac{t_s}{t}, 1+0.35\frac{L}{t}\right)$

V. CREEP-FATIGUE DAMAGE ASSESSMENT

Creep-fatigue damage assessment was conducted by cumulative damage rule [13]. In this evaluation scheme, fatigue damage ϕ_f was defined as the cycle fraction of imposed cycles N to the material's fatigue life N_f for analysed strain range as follows. The right hand expressions are provided for variable strain range case. Fatigue damage should be calculated for each strain range level denoted as $\Delta\varepsilon_{ti}$.

$$\phi_f \equiv \frac{N(\Delta\varepsilon_t)}{N_f(\Delta\varepsilon_t)}, \quad or \quad \phi_c = \sum_{i=1}^{k}\frac{N_i(\Delta\varepsilon_{ti})}{N_f(\Delta\varepsilon_{ti})} \tag{19}$$

$$\Delta\varepsilon_t = \Delta\varepsilon_e + \Delta\varepsilon_p, \quad or \quad \Delta\varepsilon_{ti} = \Delta\varepsilon_{ei} + \Delta\varepsilon_{pi} \tag{20}$$

where, $\Delta\varepsilon_t$ or $\Delta\varepsilon_{ti}$: total strain range, $\Delta\varepsilon_e$ or $\Delta\varepsilon_{ei}$:elastic strain range, $\Delta\varepsilon_p$ or $\Delta\varepsilon_{pi}$: plastic strain range, i : operation mode, k: total number of operation modes.

Low cycle fatigue life N_f was calculated by the following equation for CrMoV casting at various temperatures. This equation was obtained by the modification of the elastic part in ordinary low cycle fatigue expressions to express the unique equation for the wide range of temperatures. This equation fits the test results successfully as shown in Fig.28. If we fix the value of Young's modulus E and tensile strength σ_B at the subject temperature, we can get the conventional equation between the total strain range $\Delta\varepsilon_t$ and cycles to failure N_f [14].

$$\Delta\varepsilon_t^*(\text{in }\%) \equiv \frac{\Delta\varepsilon_e E}{100\sigma_B} + \Delta\varepsilon_p = C_e^* N_f^{\alpha_e^*} + C_p N_f^{\alpha_p} \tag{21}$$

where, C^*_e, C_p, α^*_e, α_p :regression constants as the values are shown in Fig.28.

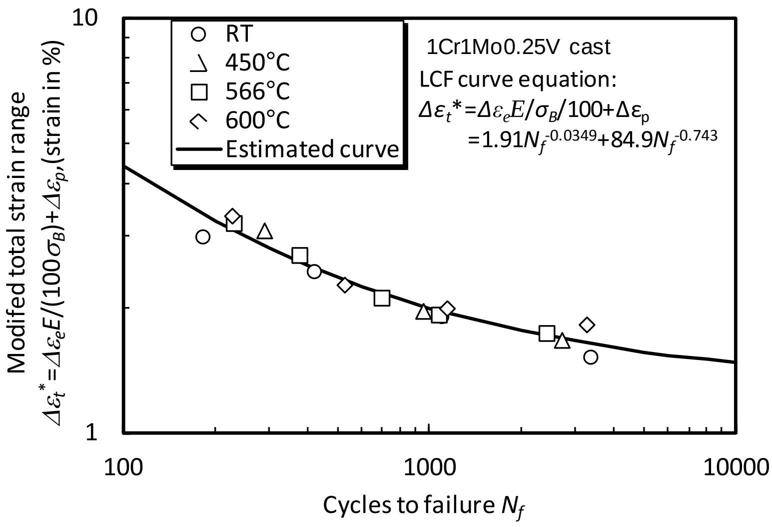

Fig. 28 Unified curve for low cycle fatigue properties

Creep damage ϕ_c was defined as the time fraction of duration hours t to the material's creep rupture life t_r as follows. For varying stress conditions the right hand integral (or summation) form could be used.

$$\phi_c \equiv \frac{t(\sigma)}{t_r(\sigma)}, \quad or \quad \phi_c = \int_0^t \frac{dt}{t_r(\sigma(t))} \tag{22}$$

Creep rupture life t_r is calculated by the following regression curve as indicated in Fig. 29. The regression form of Eq.(23) indicates the Larson-Miller parameter defined as the left hand side of the equation is expressed by the third order polynomials of the logarithm of stress-hardness ratio [14]. Instead of hardness HV, the use of tensile strength at ambient temperature can be used.

$$P \equiv T(C + \log t_r) = \sum_{i=0}^{3} A_i \left\{ \log\left(\frac{\sigma}{HV}\right) \right\}^i \tag{23}$$

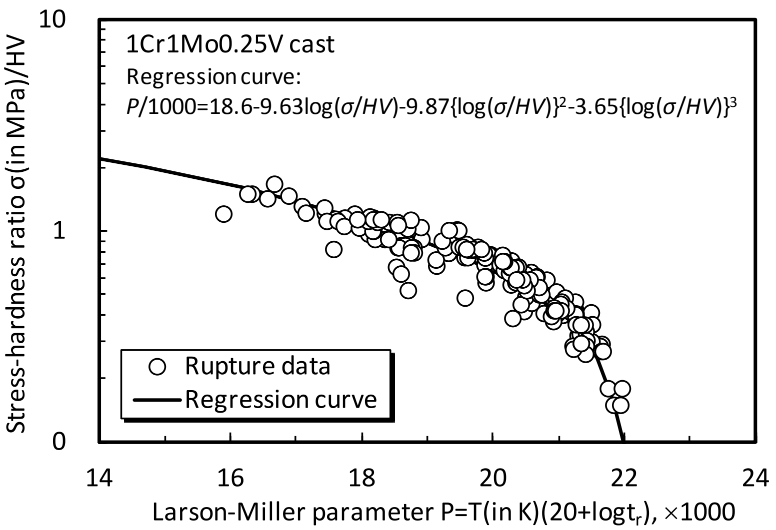

Fig. 29 Creep rupture curve

Creep-fatigue damage diagram is expressed in the following equation and shown in Fig. 30. Eq.(22) is a non-linear cumulative damage model [15] when m≠1 and n≠1. This expression has the advantage that best fit curve can be easily obtained by the least square method compared with the conventional bi-linear expressions [13]. The constant values of m and n are given in Fig.30.

$$\phi_f^m + \phi_c^n = 1 \tag{22}$$

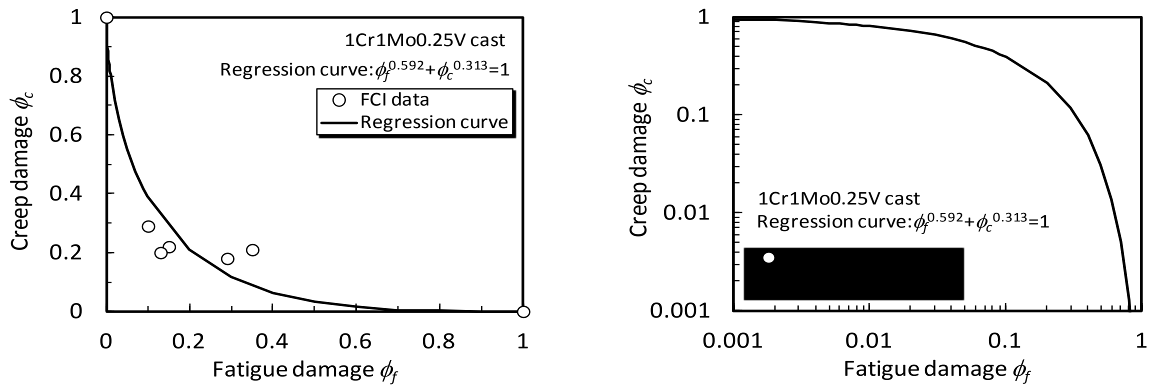

(a) Linear scale

(b) Full logarithmic scale

Fig. 30 Creep-fatigue damage diagram

VI. SHAPE OPTIMIZATION

To obtain creep-fatigue damage plots for the calculated cases, we must assume expected number of starts and operation time to calculate the fatigue and creep damage respectively. Three case studies are shown in Fig. 31. The optimum design was selected under the prescribed *t* and t_s values for each case. The optimization of *R* was conducted numerically to meet the creep-fatigue diagram expressed by Eq.(22) and the results are listed in Table IV. In these case studies, smaller values of *R* are welcomed because the design restriction can be reduced. For the case of *t*=50mm, relatively large *R* is required, but the fatigue damage is considerably small and the accuracy of the calculation could be worse. For the case of *t*=100mm, 2 or 3mm corner radius is required. For the case of *t*=150mm, larger *R* values are required to satisfy the imposed conditions. Thus, creep-fatigue optimization is proved to be achieved easily by the equations presented here.

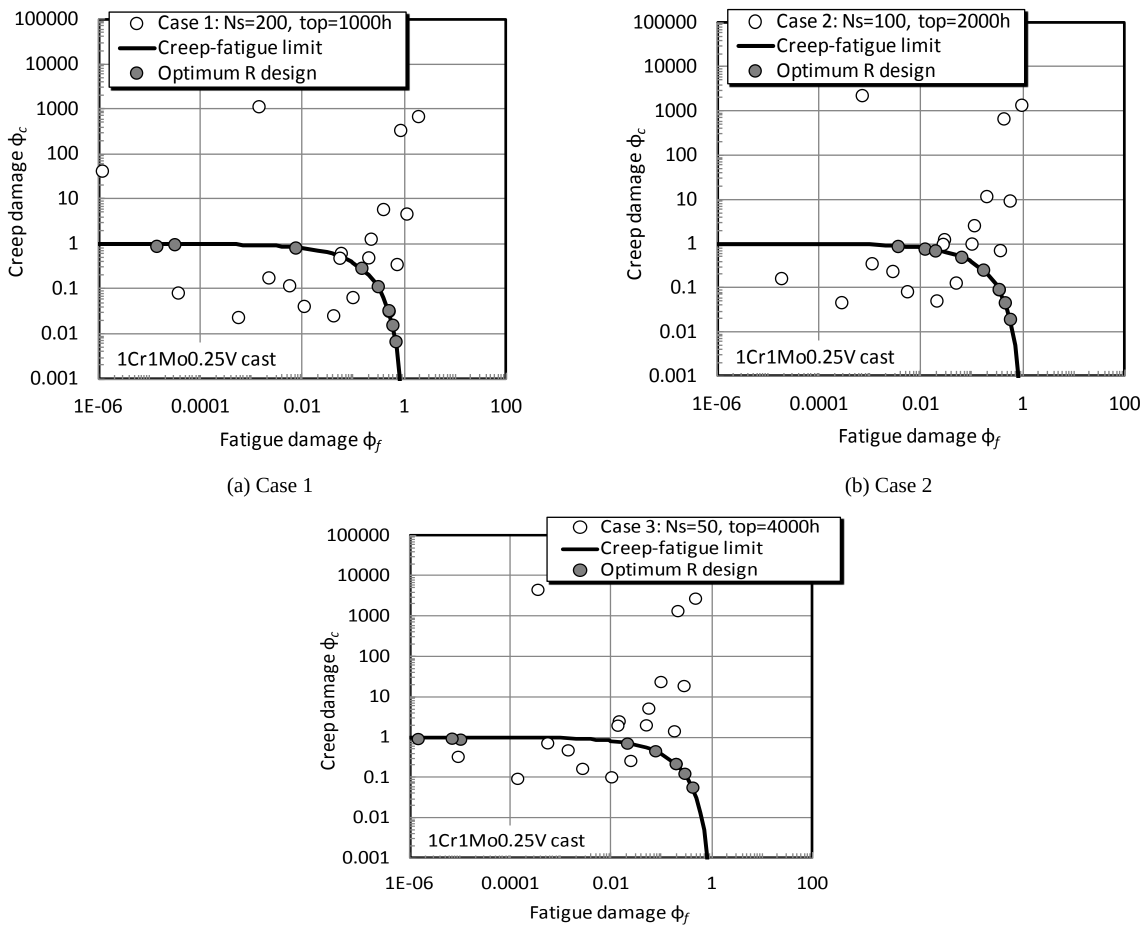

(a) Case 1

(b) Case 2

(c) Case 3

Fig. 31 Creep-fatigue damage plot for calculated results

TABLE IV OPTIMIZED *R* AND RESULTANT DAMAGE AMOUNTS

t(mm)	t_s(mm)	*R* optimized by analysis (mm) and resultant damage amounts								
		Case 1	ϕ_f	ϕ_c	Case 2	ϕ_f	ϕ_c	Case 3	ϕ_f	ϕ_c
50	60	11.0	3.0×10^{-5}	0.99	29.2	0.0035	0.89	187	1.0×10^{-5}	0.89
	75	3.7	1.3×10^{-5}	0.91	6.8	0.012	0.78	11.0	6.7×10^{-6}	0.95
	100	1.6	0.0072	0.84	2.4	0.019	0.71	3.2	1.4×10^{-6}	0.93
100	120	2.4	0.14	0.30	2.6	0.061	0.51	3.1	0.021	0.71
	150	2.4	0.30	0.12	2.2	0.16	0.26	2.4	0.075	0.46
	200	3.0	0.49	0.033	2.4	0.34	0.093	2.1	0.19	0.22
150	180	4.0	0.49	0.034	3.1	0.33	0.095	2.8	0.19	0.22
	225	4.9	0.58	0.0160	3.6	0.44	0.047	2.9	0.28	0.13
	300	6.9	0.67	0.0069	4.6	0.56	0.020	3.3	0.41	0.058

VII. CONCLUSIONS

Creep-fatigue damage evaluation procedures and shape optimization methodology were demonstrated and applied to the simple casing models of steam turbine. By assigning the fillet corner radius R as the object shape parameter, creep-fatigue damage calculations were conducted using elastic FE analysis with inelastic strain analysis by Neuber's rule and the pressure stress concentration factor. The formulation of creep and fatigue properties enabled the shape optimization for creep-fatigue conditions. The obtained fillet corner radius R strongly affected the low cycle fatigue damage accumulation as well as creep damage in this model. The application of the proposed method is not restricted to the casing model but can be applied to other structures used at high temperatures or at high stress/strain conditions for initial selection of basic design in large components.

ACKNOWLEDGMENT

The author would like to acknowledge Mr. Hiroyuki Hirano, the former post graduate student, to conduct the FE analysis.

REFERENCES

[1] K. Fujiyama, S. Nagai, Y. Akikuni, T. Fujiwara, K. Furuya, S. Matsumoto, K. Takagi and T. Kawabata, "Risk-based inspection and maintenance systems for steam turbines", Int. J. Pressure Vessels and Piping, vol. 81, pp.825-835, Elsevier Ltd., 2004.

[2] D. François, A. Pineau and A. Zaoui, *Mechanical Behaviour of Materials Vol.II: Fracture Mechanics and Damage*, Springer, 2013.

[3] R. H. Gallagher and O.C. Zienkiewicz, Ed., *Optimum Structural Design - Theory and Application -*, London, UK, John Wiley & Sons, Inc., 1973.

[4] R. W. Hertzberg, R. P. Vinci and J. L. Hertzberg, *Deformation and Fracture Mechanics of Engineering Materials, Fifth Edition*, Hoboken, USA: John Wiley & Sons, Inc., 2013.

[5] D. C. Gonyea, "Thermal stress concentration factors in large shafts", *Thermal fatigue of Materials and Components*, ASTM STP 612, American Society for Testing and Materials, pp.30-38, 1976.

[6] W. Choi, K. Fujiyama, B. Kim and G. Song, "Development of thermal stress concentration factors for life assessment of turbine casings", Int. J. Pressure Vessels and Piping, vol.98, pp.1-7, Elsevier Ltd., 2012.

[7] R. E. Peterson, *Stress Concentration Factors*, John Wiley & Sons, Inc., 1974.

[8] K. Fujiyama, private communications.

[9] K. Watashi, "The calculational method of thermal stress", The No.900-63 seminar text: *The technologies of analysis and evaluation and the measures for residual stresses and thermal stresses*, The Japan Society of Mechanical Engineers, October 1990(in Japanese).

[10] G. L. Baker and J.P. Gollub, *Chaotic Dynamics an introduction*, Cambridge University Press, 1990.

[11] K. Kimura, K. Fujiyama and M. Muramatsu, "Creep and Fatigue Life Prediction Based on the Non-destructive Assessment of Material Degradation for Steam Turbine Rotors", *High Temperature Creep-Fatigue, Current Japanese Materials Research,* vol.3, pp.247-270, Elsevier Applied Science Publishers LTD, UK and the Society of Materials Science, Japan, 1988.

[12] K. Maruyama and H Nakajima, *Materials Science for High Temperature Strength - Creep Theory and Its Application to Engineering Materials - Revised Edition*, Uchida Rokakuho Publishing Co., LTD., November 2002.

[13] S. S. Manson and G. R. Halford, *Fatigue and Durability of Metals at High Temperatures*, ASM International, Ohio, USA, July 2009.

[14] K. Fujiyama, T. Fujiwara, Y. Nakatani, K. Saito, A. Sakuma, Y. Akikuni, S. Hayashi and S. Matsumoto, Acta Metallurgica Sinica, vol.17, No.4, pp.338-344, August 2004.

[15] K. Fujiyama, T. Shima, T. Muraoka and Y. Mizuno, "The statistical material selection and structural design maps for high temperature components", *Proc. PVP2007*, ASME, San Antonio, USA, pp.1-8, July 2007.

Kazunari. Fujiyama was born in Kyoto prefecture, Japan on 7 September 1954. He was graduated from Kyoto University in Japan in 1977 and obtained Master of Engineering from Kyoto University postgraduate school in 1979. He earned Doctor of Engineering from Kyoto University in 1998. His major field of study is the strength of materials especially at high temperatures from reliability engineering aspects.

Before joining Meijo University in 2005, he was employed by Toshiba Corporation for 26 years at Turbine Material & Strength R&D section of Heavy Apparatus Engineering Laboratory in Keihin Product Operations. As a Chief Specialist, he was engaged in life assessment technology development for steam turbines, gas turbines and HRSGs. Currently, he is a Professor of Mechanical Engineering in Meijo

University, Nagoya, Japan. Previous publications:1) K. Fujiyama, “Chapter 1: Crystallographic Observation and Delamination Damage Analyses for Thermal Barrier Coatings Under Thermal Exposure”, in “Crystallization and Materials Science of Modern Artificial and Natural Crystals”, Ed. by E. Borisenko and N. Kolesnikov, Intech, Croatia, pp.1-22, Jan. 2012., 2) K. Fujiyama, H. Kimachi, Y. Watanabe, K. Hijikuro and T. Tsuboi: “The concept of ‘EBSD strain analysis’ and its application to creep and creep-fatigue damage assessment of ferritic and austenitic heat resistant steels”, Strength, Fracture and Complexity, vol.7, pp.123-125, Sendai, Japan, 2011., 3) K. Fujiyama, H.Kimachi, T. Tsuboi, H. Hagiwara, S. Ogino and Y. Mizutani, “Damage Assessment of Heat Resistant Steels through Electron BackScatter Diffraction Strain Analysis under Creep and Creep-Fatigue Conditions”, Journal of Solid Mechanics and Materials Engineering, vol.6, No.6, JSME, Japan, June 2012. His research interests are high temperature strength of materials and life assessment of large components, especially focused on crystallographic and microscopic damage observation and analysis and risk-based engineering application for design and maintenance planning of turbines.

Dr. Fujiyama is JSME(the Japan society of Mechanical Engineers) fellow since 2005, a member of JSMS(the Society of Materials Science, Japan) and a member of GTSJ(Gas Turbine Society of Japan). He earned License of Professional Engineer, Japan, May 2003, for Mechanical Engineering and Comprehensive Technical Management. Some of obtained awards are 1)GTSJ outstanding paper award in 2004 and 2008, 2)JSME Materials and Mechanics Division outstanding activity medal in 2012, 3)JSMS Branch distinguished conduct medal in2013.